

Benchmarking Turbulence Models to Represent Cloud-Edge Mixing

Johannes Kainz¹, Nikitabahen N. Makwana², Bipin Kumar²,
S. Ravichandran³, Johan Fries⁴, Gaetano Sardina⁵,
Bernhard Mehlig^{4,5}, Fabian Hoffmann¹

¹Ludwig-Maximilians-Universität München, Germany

²Indian Institute of Tropical Meteorology Pune, India

³Centre for Climate Studies, Indian Institute of Technology Bombay, India

⁴Gothenburg University, Sweden

⁵Chalmers University of Technology, Sweden

Key Points:

- Small-scale mixing of a cloudy filament with dry air is simulated using direct numerical simulations and statistical turbulence models.
- Statistical turbulence models capture the development of thermodynamics during cloud-edge mixing as well as direct numerical simulations.
- Changes in cloud microphysics are represented correctly only if the statistical models consider the spatial variability of supersaturation.

Abstract

Considering turbulence is crucial to understanding clouds. However, covering all scales involved in the turbulent mixing of clouds with their environment is computationally challenging, urging the development of simpler models to represent some of the processes involved. By using full direct numerical simulations as a reference, this study compares several statistical approaches for representing small-scale turbulent mixing. All models use a comparable Lagrangian representation of cloud microphysics, and simulate the same cases of cloud-edge mixing, covering different ambient humidities and turbulence intensities. It is demonstrated that all statistical models represent the evolution of thermodynamics successfully, but not all models capture the changes in cloud microphysics (cloud droplet number concentration, droplet mean radius, and spectral width). Implications of these results for using the presented models as subgrid-scale schemes are discussed.

Plain Language Summary

Although small-scale turbulence is crucial to the development of clouds, the representation of its effects is challenging. Solving the underlying fluid dynamics and cloud microphysical processes on all relevant length- and timescales is possible and highly accurate (so-called direct numerical simulations), but requires enormous computational resources. Therefore, simplified models are used to mimic the effects of small-scale turbulence. Here, we compare four approaches of different complexity to the results from direct numerical simulations. While simpler models capture changes in thermodynamic quantities successfully, the adequate consideration of spatial dependencies is shown to be necessary to represent the development of cloud droplets.

1 Introduction

Today, although considerable progress has been made in understanding the Earth’s climate system, the role of clouds still raises questions. One reason for this lack of understanding is that clouds are a multi-scale and multi-process system, ranging from the large-scale organization of cloud fields (~ 100 km) to the smallest scales of turbulence (~ 1 mm), with which aerosols, cloud droplets, and precipitation interact ($\sim 1\text{--}1000$ μm) (Bodenschatz et al., 2010).

Due to computational constraints, most modeling of the atmosphere focuses on scales larger than 100 m, while smaller-scale processes are parameterized. One of these processes is the mixing of cloudy and cloud-free air (Baker & Latham, 1979), which can change the cloud microphysical composition and hence the role of clouds in Earth’s radiation budget (Hoffmann, 2023). The mixing is termed *homogeneous* if the liquid water mixing ratio (q_c) decreases by evaporating all cloud droplets partially, that is, reducing their size but not their number concentration (N_c). During extreme *inhomogeneous* mixing, q_c is reduced by evaporating individual droplets completely, while leaving others unblemished. Thus, N_c decreases, but not the mean droplet size. It is important to note that in both cases, N_c must eventually decrease by the dilution caused by the mixing with entrained air.

In nature, mixing is usually constrained to the interface of cloudy filaments reaching into subsaturated air. If this filament is not resolved by the model, mixing becomes instantaneous and affects all droplets located in a model grid box simultaneously, which forces mixing to be preferentially homogeneous (e.g., Kainz & Hoffmann, 2023). Direct numerical simulations (DNSs), which represent all relevant scales of small-scale turbulence, may be applied to study cloud-edge mixing but are constrained to small domains of up to a meter due to the commensurately large computational requirements (Kumar et al., 2012, 2013, 2014). To address larger scales, large-eddy simulations (LESs) are commonly applied, which avoid high spatial and temporal resolution by representing dynam-

ics only on scales larger than tens to hundreds of meters, while parameterizations are used to consider the effects of unresolved scales on the resolved flow (Smagorinsky, 1963; Deardorff, 1980). A key challenge is that unresolved turbulence not only affects the dynamics. Other parameterizations are necessary to represent, for instance, the effect of turbulent supersaturation fluctuations on the condensational growth of cloud droplets (e.g., Hoffmann & Feingold, 2019).

In this study, we compare different statistical turbulence models and investigate how well they describe the condensation and evaporation of cloud droplets during the mixing of cloudy and cloud-free air. We consider the one-dimensional linear eddy model (LEM) (Kerstein, 1988), and three supersaturation-fluctuation models (Pope, 1994). The first one is the eddy-hopping model (EHM) (Pope, 1994; Grabowski & Abade, 2017; Abade et al., 2018), which models supersaturation fluctuations as an Ornstein-Uhlenbeck process (Uhlenbeck & Ornstein, 1930). The second model approximates supersaturation fluctuations at the cloud-edge by relaxation to a space-dependent mean (relaxation-to-mean model; RMM) (Pope, 2000; Fries et al., 2021). The third model rests on the mapping-closure approximation (mapping-closure model; MCM) (Chen et al., 1989; Pope, 1991; Fries et al., 2023). The LEM and EHM have already been used to represent subgrid-scale supersaturation fluctuations in LESs (Hoffmann & Feingold, 2019; Chandrakar et al., 2021). Fries et al. (2021) employed the RMM to estimate the degree of inhomogeneous mixing in the data of Beals et al. (2015). The MCM was bench-marked against a DNS of Kumar et al. (2012).

Until now, there have been no systematic studies comparing the strengths and weaknesses of the LEM, EHM, RMM, and MCM. Thus, in the present study we

- compare all models mentioned above against each other, and with a set of new reference DNSs based on Kumar et al. (2014),
- test to which extent the models describe the thermodynamical and cloud microphysical responses to different turbulence intensities and ambient humidities, and
- discuss aspects necessary to consider when the different approaches are used as subgrid-scale models.

The paper is organized as follows. First, each model is introduced, and the case setups are presented. Then, two sensitivity studies, one assessing the effect of turbulence intensity and one ambient humidity, are discussed. Differences between the models are highlighted and the applicability of the models as subgrid-scale schemes is discussed. We then conclude with remarks on future work.

2 Models

The main way cloud microphysics and dynamics interact is through supersaturation, which drives the condensation and evaporation of cloud droplets. The relative supersaturation with respect to liquid water can be defined as

$$S(\mathbf{x}, t) = \frac{q_v(\mathbf{x}, t)}{q_{vs}[T(\mathbf{x}, t), p]} - 1, \quad (1)$$

and is determined by the water vapor mixing ratio q_v and absolute temperature T , where q_{vs} is the saturation water vapor mixing ratio, and p is the hydrostatic pressure. Fundamentally, S is a field, defined at any point in space \mathbf{x} and time t . Supersaturation fluctuations are shaped by the advection of q_v and T , as well as sinks and sources, e.g., the condensation and evaporation of cloud droplets.

All models used in this study aim to determine the spatial and temporal fluctuations of S . The most fundamental approach is DNS, described first, followed by short introductions to the LEM, EHM, RMM, and MCM, which idealize the underlying pro-

cesses to different degrees. Note that the following descriptions cannot provide the depth necessary to understand each approach completely. Thus, references are given to guide the interested reader to further information.

2.1 Direct Numerical Simulation (DNS)

DNSs are the most accurate approach to investigate the dynamics of fluids (Moin & Mahesh, 1998), and have been adapted to investigate clouds in the last decades (e.g., Vaillancourt et al., 2001). The applied DNS model is described in Kumar et al. (2014, 2017). To predict the velocity of air \mathbf{u} , where bold font indicates a three-dimensional vector, the DNS solves the incompressible, Oberbeck-Boussinesq-approximated Navier-Stokes equations. These are

$$\frac{\partial \mathbf{u}}{\partial t} + (\mathbf{u} \cdot \nabla) \mathbf{u} = -\frac{1}{\rho_0} \nabla p + \nu \nabla^2 \mathbf{u} + \mathbf{B} + \mathbf{f}_{\text{LS}}, \quad (2)$$

where ∇ and $\partial/\partial t$ denote spatial and temporal derivatives, ρ_0 a reference air density, and ν the kinematic viscosity of dry air. \mathbf{B} is the buoyancy force (Eq. (6) in Kumar et al., 2014), and \mathbf{f}_{LS} a large-scale forcing driving the flow in a statistically stationary fashion (Eq. (7) in Kumar et al., 2014).

The thermodynamic fields T and q_v obey

$$\frac{\partial T}{\partial t} + \mathbf{u} \cdot \nabla T = D_\kappa \nabla^2 T + \frac{l_v}{c_p} C_d, \quad (3a)$$

$$\frac{\partial q_v}{\partial t} + \mathbf{u} \cdot \nabla q_v = D_v \nabla^2 q_v - C_d, \quad (3b)$$

where D_κ is the molecular diffusivity of heat, D_v molecular diffusivity of water vapor, l_v the enthalpy of vaporization, c_p the specific heat of air at constant pressure. Note that Eq. (3a) does not consider the cooling or warming due to vertical motions, as this term is negligible for the limited vertical domain considered in this study. To ease comparison, this term is not considered in the models described below. The effect of condensation and evaporation on T and q_v in Eqs. (3) is considered by

$$C_d(\mathbf{x}, t) = \frac{4}{3} \pi \frac{\rho_l}{\rho_0} \sum_{\alpha}^N \frac{G(\mathbf{x} - \mathbf{x}_\alpha; \Delta V)}{\Delta V} \frac{dr_\alpha^3}{dt}. \quad (4)$$

Here, x is a location vector and \mathbf{x}_α the location of a cloud droplet α , which radius growth rate by condensation is dr_α/dt . The number of all droplet is given by N . ρ_l is the density of liquid water. The spatial kernel G is unity in a volume ΔV around \mathbf{x} , and zero otherwise. For DNS, ΔV is identical to the volume of a DNS grid cell.

Cloud droplet dynamics are described in a Lagrangian fashion, as heavy spherical inertial particles (Bec et al., 2024). In the Stokes approximation, their equations of motion read

$$\frac{d\mathbf{x}_\alpha}{dt} = \mathbf{v}_\alpha, \quad (5a)$$

$$\frac{d\mathbf{v}_\alpha}{dt} = \frac{1}{\tau_s} [\mathbf{u}(\mathbf{x}_\alpha) - \mathbf{v}_\alpha] - \mathbf{g}, \quad (5b)$$

where \mathbf{v}_α is the droplet velocity and $\mathbf{u}(\mathbf{x}_\alpha)$ the air velocity at the droplet's location. \mathbf{g} describes the acceleration due to gravity. The influence of drag is considered by the particle-response time in Stokes approximation, $\tau_s = 2\rho_l r_\alpha^2 / (9\rho_0 \nu)$, where r_α is the radius the considered droplet.

The change in droplet radius due to evaporation and condensation is modeled as

$$r_\alpha \frac{dr_\alpha}{dt} = KS(\mathbf{x}_\alpha, t), \quad (6)$$

which is primarily driven by S determined from T and q_v via Eq. (1) at \mathbf{x}_α . The growth rate is scaled by $K = 1/[\rho_l(K_D + K_\kappa)]$, with $K_D = R_v T/[e_s(T)D_v]$ considering the transport of water vapor, and $K_\kappa = [l_v/(R_v T) - 1] l_v/(\kappa T)$ the conduction of heat. Here, R_v is the gas constant of water vapor, $e_s(T)$ the saturation vapor pressure, and κ the thermal conductivity of air.

2.2 Linear-Eddy Model (LEM)

The LEM is a statistical turbulence model developed by Kerstein (1988), and was introduced to cloud physics by Krueger (1993). The LEM deviates from DNS by utilizing a one-dimensional description of inertial-range turbulence, in terms of an idealized mapping approach.

As such, the model does not predict the turbulent fluid velocity, but directly prescribes the relocation of scalars as

$$T(x, t + dt) = T[M(x), t], \quad (7a)$$

$$q_v(x, t + dt) = q_v[M(x), t]. \quad (7b)$$

The mapping M mimics turbulent stretching and folding, i.e., it steepens gradients in T and q_v , with the exact mathematical treatment shown in, e.g., Eq. (10.2) by Menon and Kerstein (2011). M is applied with a probability of dt/τ_{LEM} , with τ_{LEM} the average time between two turbulent eddies mixing the domain. τ_{LEM} is determined from inertial range scaling using the outer scale of turbulence L and the kinetic energy dissipation rate ε , as well as the domain size L_x (Eq. (2.4) in Krueger, 1993). M places an eddy at a random location in the domain, and its size l is randomly chosen from the spectrum of eddy lengths in the inertial subrange, bounded by L_{outer} and the Kolmogorov lengthscale η (Eq. (2.3) in Krueger, 1993), which describes the smallest scale of motion in the flow. Below this scale, molecular diffusion is the dominant driver of energy dissipation.

The evolution of T and q_v by molecular diffusion and condensation is described by

$$\frac{\partial T}{\partial t} = D_\kappa \frac{\partial^2 T}{\partial x^2} + \frac{l_v}{c_p} C_d, \quad (8a)$$

$$\frac{\partial q_v}{\partial t} = D_v \frac{\partial^2 q_v}{\partial x^2} - C_d. \quad (8b)$$

Compared with the DNS Eqs. (3), Eqs. (8) miss the advection term on their left-hand sides, which is considered in the LEM via M in Eqs. (7). Note that although the LEM is one-dimensional by design, its grid boxes are three-dimensional to represent droplet-concentration-dependent processes correctly. Thus, C_d is evaluated as in the DNS with the reference volume matching the volume of a LEM grid box.

It is assumed that cloud droplets move with the surrounding fluid. Thus, their location changes as

$$x_\alpha(t + dt) = x[M(x_\alpha)], \quad (9)$$

utilizing the same mapping considered in Eqs. (7). While this is a simplification the following models heavily rely on, it is not a necessary requirement for the LEM, in which it is possible to consider sedimentation or inertia effects that could decouple the motion of droplets from the motion of the fluid (Krueger & Kerstein, 2018). These effects are neglected in the present study.

Droplet condensational growth is determined as

$$r_\alpha \frac{dr_\alpha}{dt} = KS(x_\alpha). \quad (10)$$

Similar to DNS, S is determined from T and q_v via Eq. (1) but at x_α , the droplet's location in one-dimensional space. This constitutes a minor difference to DNS, where S is evaluated in three-dimensional space.

2.3 Eddy-Hopping Model (EHM)

The EHM is a statistical model originally suggested by Pope (1994), and applied by Grabowski and Abade (2017) and Abade et al. (2018) to studying the broadening of droplet size distributions. The model was improved by Saito et al. (2021), who reduced the number of model variables, while keeping the capability to reproduce the scaling of the model parameters unchanged. In the EHM, the evolution of individual fluid elements is predicted and it is assumed that cloud droplets move with those fluid elements.

First, prognostic equations for the domain-averaged T and q_v are solved as

$$\frac{\partial \bar{T}}{\partial t} = \frac{l_v}{c_p} C_d, \quad (11a)$$

$$\frac{\partial \bar{q}_v}{\partial t} = -C_d, \quad (11b)$$

where $\bar{(\cdot)}$ indicates the domain average. Because \bar{T} and \bar{q}_v are domain-averaged quantities, advection and molecular diffusion are not considered, and the reference volume to determine C_d encloses the entire domain. From \bar{T} and \bar{q}_v , the desired \bar{S} is determined via Eq. (1).

A perturbation from \bar{S} is predicted for Lagrangian fluid elements by

$$\frac{dS'_\alpha}{dt} = -C_{\text{EHM},1} \frac{S'_\alpha}{\tau_L} - C_{\text{EHM},2} \frac{S'_\alpha}{\tau_p}. \quad (12)$$

The first term represents changes in S'_α due to turbulent mixing, steered by the integral timescale of turbulence

$$\tau_L = \left(\frac{L_{\text{outer}}^2}{\varepsilon} \right)^{1/3}.$$

The second term depicts changes due to condensation or evaporation by S'_α , and is derived from C_d . The rate of condensation or evaporation is the phase relaxation timescale

$$\tau_p = \frac{1}{a_S a_K r_m N_c},$$

which is determined from the average droplet radius r_m , the domain-averaged droplet concentration mixing ratio N_c , with $a_S = [1/q_v + l_v^2/(c_p R_v T^2)]$ and $a_K = 4\pi\rho_l K$. Note that the parameters $C_{\text{EHM},1}$ and $C_{\text{EHM},2}$ are tuning parameters to fit the model to the DNS results (Saito et al., 2021).

By combining \bar{S} and S'_α , the growth of droplets is expressed as

$$r_\alpha \frac{dr_\alpha}{dt} = K(\bar{S} + S'_\alpha). \quad (13)$$

Thus, condensational growth is determined by S'_α , i.e., a quantity immanent to a specific Lagrangian fluid element. This constitutes a fundamental difference to the representation of condensational growth in DNS and LEM, in which S is evaluated at a specific location in space.

2.4 Relaxation-to-Mean Model (RMM)

Fries et al. (2021) derived a one-dimensional statistical model, which thermodynamics are not determined by T and q_v , but S directly. Note that we do not show the non-dimensional equations of Fries et al. (2021) to ease comparison with the other models presented here.

In the RMM, two types of Lagrangian fluid elements are simulated, those that contain droplets and those that do not. It is assumed that the droplets move with the fluid elements, and their motion is described by the Langevin equation

$$du_\alpha = -\frac{u_\alpha}{\frac{4}{3}\tau_L/C_0}dt + (\tau_L\varepsilon C_0)^{1/2} dW. \quad (14)$$

The first term describes the autocorrelation of a fluid element's motion, with $\frac{4}{3}\tau_L/C_0$ the autocorrelation timescale (Fries et al., 2021), and the parameter C_0 according to Pope (2011). The second term represents turbulent motion as Brownian increments, with dW being an increment of a Wiener process with zero mean and variance, dt/τ_L , equal to a time step (Pope, 1991). $(\tau_L\varepsilon C_0)^{1/2}$ is the standard deviation of the velocity increments. The displacement of a fluid element is given by

$$\frac{dx_\alpha}{dt} = u_\alpha. \quad (15)$$

Similar to Eq. (12) in the EHM, S_α is determined by

$$\frac{dS_\alpha}{dt} = -C_{\text{RMM},1} \frac{S_\alpha - \langle S(x_\alpha, t) \rangle}{\tau_L} - C_{\text{RMM},2} \frac{\langle r(t)S(x_\alpha, t) \rangle / r_i}{\tau_{p,i}}. \quad (16)$$

The first term describes the relaxation of S_α to $\langle S(x_\alpha, t) \rangle$, the ensemble-averaged S determined from all simulated fluid elements at t and x_α (Fries et al., 2021). The ensemble average is indicated by $\langle \cdot \rangle$. The second term describes the effect of condensation and evaporation, and can be derived from C_d . Similar to the first term, $\langle r(t)S(x_\alpha, t) \rangle$ is an ensemble-average determined from all simulated fluid elements at t and x_α . Here, r_i and $\tau_{p,i}$ are the initial droplet radius and phase relaxation timescale, respectively. $C_{\text{RMM},1}$ and $C_{\text{RMM},2}$ are empirical constants.

Droplet condensational growth is determined as

$$r_\alpha \frac{dr_\alpha}{dt} = K S_\alpha, \quad (17)$$

similar to EHM. However, S_α is linked to a x_α , which enables RMM to consider spatial information of the mixing process that is missing in the EHM.

2.5 Mapping-Closure Model (MCM)

For a better representation of supersaturation fluctuations, Fries et al. (2023) developed another statistical mixing model based on the mapping-closure approach by Chen et al. (1989) and Pope (1991).

Similar to the RMM, the MCM is based on replacing T and q_v with a single equation for S ,

$$\frac{\partial S}{\partial t} + \mathbf{u} \cdot \nabla S = D \nabla^2 S + \frac{1}{q_{vs}(T_0, p_0)} C_d, \quad (18)$$

where T_0 and p_0 are reference temperatures and pressures, respectively. To retrieve S , MCM does not solve Eq. (18) directly, but employs a mapping X from a time-independent Gaussian-distributed random variable $\xi(t)$, with zero mean and unit variance, to $S(\mathbf{x}, t)$,

Table 1. Parameters for the initial T , q_v , and S profiles.

	T_e (K)	$q_{vs,e}$ (g kg ⁻¹)	$q_{v,e}$ (g kg ⁻¹)	S_e (-)	T_c (K)	$q_{vs,c}$ (g kg ⁻¹)	$q_{v,c}$ (g kg ⁻¹)	S_c (-)
n_0	271.4099	4.048	0.031	-0.9922	270.7535	3.866	4.015	0.03852
n_1	271.3074	4.019	1.027	-0.7444	270.8151	3.883	4.015	0.03403
n_2	271.2049	3.990	2.023	-0.4929	270.8768	3.899	4.015	0.02957
n_3	271.1025	3.962	3.019	-0.2379	270.9384	3.916	4.015	0.02513

which — in a statistical sense — is interpreted as an *arbitrarily* distributed random variable. Accordingly, for a given \mathbf{x} and t ,

$$S(\mathbf{x}, t) = X\{\xi[\mathbf{x}/\lambda_{\text{MCM}}(t)], t\}, \quad (19)$$

where $\lambda_{\text{MCM}}(t)$ a time-dependent length scale. By inserting Eq. (19) in (18), with some further considerations detailed in Fries et al. (2023), X is predicted as

$$\frac{\partial X}{\partial t} = \varphi(t) \left(-\delta \frac{\partial X}{\partial \delta} + \frac{\partial^2 X}{\partial \delta^2} \right) - \frac{\tau_L}{\tau_{p,i}} \langle C_d | S = X \rangle, \quad (20)$$

where δ is the sample-space variable corresponding to ξ , with the sample space containing all possible realizations of ξ . Further, $\varphi(t)$ is a relaxation rate, and $\langle C_d | S = X \rangle$ is a conditional ensemble-averaged condensation rate. $\varphi(t)$ and the aforementioned $\lambda_{\text{MCM}}(t)$ are *unknown* for most applications. Hence, they are determined from DNS here, while theoretical closures may exist for specific cases.

Similar to Eqs. (12) and (16) in EHM and RMM, MCM predicts ξ_α for multiple fluid elements using a Langevin equation, such that

$$d\xi_\alpha = -R(t)\xi_\alpha dt + \sqrt{2R(t)} dW. \quad (21)$$

This approach ensures that the ensemble of ξ_α relaxes to a Gaussian as assumed for ξ above. Moreover, Fries et al. (2023) set $R(t) = C_{\text{MCM}}\varphi(t)$, with C_{MCM} a fitting parameter from DNS.

Similar to EHM and RMM, the droplet condensational growth equation is

$$r_\alpha \frac{dr_\alpha}{dt} = KX(\xi_\alpha, t). \quad (22)$$

Here, however, the mapping X is crucial to determine S from ξ_α via Eq. (19).

3 Case Setup

We simulate the mixing of a cloudy filament with dry air. In this section, we will summarize the setup of the simulated cases, and how the different models are initialized.

3.1 Simulated Cases

All models simulate a domain that is characterized by the lengthscale $L_x = 51.2$ cm, irrespective of the dimensionality of the considered approach. All simulations are run for 40 s. Without the aim to simulate a specific cloud type, we prescribe reference values typical for low-level clouds (e.g., shallow cumulus or stratocumulus), with $T_0 = 271$ K, $\rho_0 = 1.06$ kg m⁻³, and $p_0 = 824.6$ hPa.

Table 2. Turbulence parameters used in this study.

ε	($\text{cm}^2 \text{s}^{-3}$)	1	10	33.75	100	1000
TKE	($\text{cm}^2 \text{s}^{-2}$)	7	34.4	78.8	168.1	799.9
τ_L	(s)	7	3.44	2.34	1.68	0.8

To represent the mixing of a cloudy filament with dry air, we initialize q_v and T such that they depict the change from dry to cloudy air along each model's primary dimension, following the original setup proposed by Kumar et al. (2014). We assume that the model's primary dimension is the x -axis. Thus,

$$q_{v,i}(x) \equiv q_v(x, t = 0) = (q_{v,c} - q_{v,e}) \exp \left[-\lambda \left(x - \frac{L_x}{2} \right)^8 \right] + q_{v,e}, \quad (23)$$

with $q_{v,e}$ the minimum of q_v found in the environment, $q_{v,c}$ the maximum of q_v inside the cloud, and $\lambda = 1.45 \times 10^{-10} \text{cm}^{-8}$. The T profile is

$$T_i(x) \equiv T(x, t = 0) = T_0 \left\{ 1 - \left(\frac{R_v}{R_d} - 1 \right) [q_{v,i}(x) - q_{v,e}] \right\}, \quad (24)$$

where R_d is the gas constant of dry air. The corresponding initial S_i profile is determined from $q_{v,i}$ and T_i via Eq. (1).

To investigate the impact of ambient humidity, we vary $q_{v,i}$ by adapting $q_{v,e}$ as

$$q_{v,e} = q_{v,e}^{\text{original}} + n \frac{q_{v,c} - q_{v,e}^{\text{original}}}{4}, \quad (25)$$

with n from 0 to 3, and $q_{v,e}^{\text{original}}$ taken from Kumar et al. (2014). The corresponding setups are called n_0 to n_3 , respectively. The resultant values for T , q_v , q_{vs} , and S in the environment (subscript e) and in the cloud (subscript c) are summarized in Tab. 1. To assess the impact of turbulence, ε is varied between 1 and $1000 \text{cm}^2 \text{s}^{-3}$, with the corresponding turbulence parameters stated in Tab. 2.

Cloud droplets are initialized as monodisperse particles with initial radii $r_i = 5$ or $15 \mu\text{m}$ in the the central 22 cm of the domain. We refer to this part of the domain as the *cloudy part*. Note that although the cloudy part covers most of the supersaturated domain, these regions are not identical due to the varying ambient humidity. For all cases, the same domain-averaged $N_{c,i} = 47 \text{mg}^{-1}$ is initialized, corresponding to 109mg^{-1} in the cloudy part. This results in $q_{c,i} = 0.06 \text{g kg}^{-1}$ or 1.54g kg^{-1} for $r_i = 5$ or $15 \mu\text{m}$ in the cloud part. Figure 1 summarizes the initial profiles for $q_{v,i}$, T_i , S_i , and $q_{c,i}$ for all thermodynamic setups (n_0 to n_3) and r_i .

All models use the parameters summarized in Tab. 3. Moreover, to ease comparability, all models use the same

$$q_{vs}(T, p) = \frac{R_d}{R_v} \frac{e_s(T)}{p - e_s(T)} \approx \frac{R_d}{R_v} \frac{e_s(T)}{p}, \quad (26)$$

with

$$e_s(T) = b_{s,1} \exp \left(-\frac{b_{s,2}}{T} \right), \quad (27)$$

and the parameters $b_{s,1} = 2.53 \times 10^8 \text{kPa}$ and $b_{s,2} = 5420 \text{K}$ from Rogers and Yau (1989).

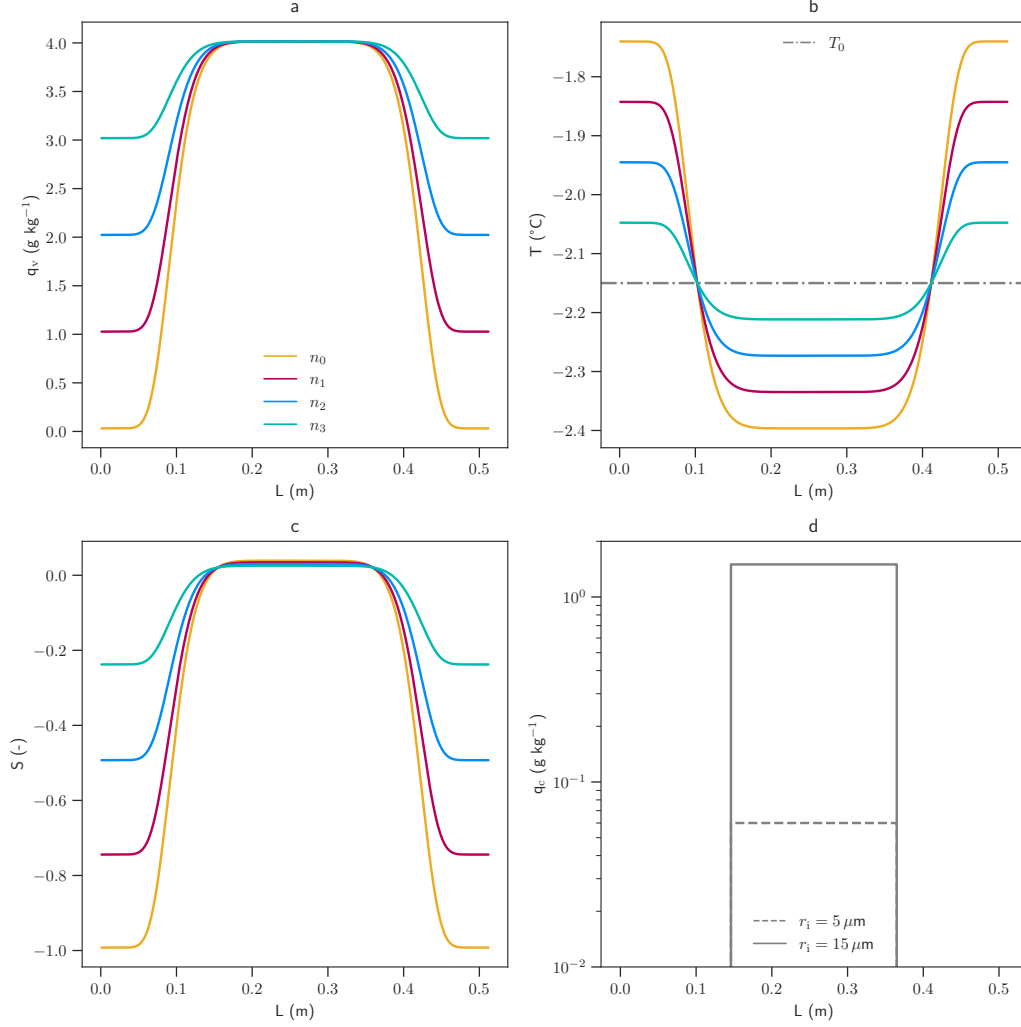


Figure 1. Initial (a) $q_{v,i}$, (b) T_i , (c) S_i , and (d) $q_{c,i}$ profiles for different thermodynamics (denoted n_0 - n_3 , colored lines) or r_i (gray lines). In (b), the reference temperature T_0 is shown (gray dashed-dotted line).

Table 3. Further parameters used in this study.

quantity	symbol	unit	value
Kinematic viscosity	ν	m ² s ⁻¹	1.5×10^{-5}
Molecular diffusivity of heat	D_κ	m ² s ⁻¹	2.23×10^{-5}
Molecular diffusivity of water vapor	D_v	m ² s ⁻¹	2.16×10^{-5}
Enthalpy of vaporization	l_v	J kg ⁻¹	2.5×10^6
Specific heat of air at const. pressure	c_p	J K ⁻¹ kg ⁻¹	1005.0
Density of liquid water	ρ_l	kg m ⁻³	1000.0
Gas constant of water vapor	R_v	J K ⁻¹ kg ⁻¹	461.5
Gas constant of dry air	R_d	J K ⁻¹ kg ⁻¹	287.0
Thermal conductivity	κ	J m ⁻¹ s ⁻¹ K ⁻¹	2.38×10^{-2}

3.2 Model Initialization

In DNS and LEM, the initial distributions of $q_{v,i}$, T_i , and hence S_i are represented on a numerical grid with resolutions of 1.0 and 0.1 mm, and 134 217 728 and 5 120 grid boxes, respectively. In the initially cloudy part of the domain, the approaches initialize 6 771 519 and 2 594 Lagrangian cloud droplets at random $\mathbf{x}_{\alpha,i}$ and $x_{\alpha,i}$, respectively. For DNS and LEM, $r_{\alpha,i} = r_i$ for all simulated droplets initially.

For EHM, \overline{S}_i is determined from \overline{T}_i and $\overline{q_{v,i}}$. $S'_{\alpha,i}$ is calculated such that $\overline{S}_i + S'_{\alpha,i} = S_i(x_i)$, where x_i are randomly picked locations in the cloudy region. (Note that x_i is only relevant during the initialization, and is not considered in subsequent calculations of the EHM.) In total, 2,594 Lagrangian cloud droplets are simulated, with their initial $r_{\alpha,i} = r_i$.

RMM assigns $S_{\alpha,i} = S_i(x_{\alpha,i})$ to Lagrangian fluid elements at random locations $x_{\alpha,i}$. The fluid elements are of two types, representing air with or without droplets, respectively. 1.4×10^5 air elements are initialized in the entire domain, 2×10^5 droplet elements within the cloudy part. The latter are assigned the radius $r_{\alpha,i} = r_i$, while the prior $r_{\alpha,i} = 0$ throughout the simulation.

MCM determines the initial mapping X_i from the relation $F_i[X_i(\delta)] = \Gamma(\delta)$, where $F_i(S)$ is the initial cumulative distribution function (CDF) of S from DNS, and $\Gamma(\dots)$ is the CDF of a standardized Gaussian-distributed variable. One proceeds by sampling 10^6 fluid elements with $\xi_{\alpha,i}$ from a standardized Gaussian conditional on that they are mapped to a supersaturation $X_i(\xi_{\alpha,i})$ found within the droplet-containing region of the initially cloud part of the domain. The fluid elements are assigned the initial radius $r_{\alpha,i} = r_i$.

Simulations using the LEM and EHM are repeated each 1000 times to gain reliable ensemble averages. Because RMM and MCM compute a much larger number of fluid elements, ensemble-averaging is not necessary. Also for DNS, results from only one simulation are considered.

4 Results

4.1 General Development

The qualitative behavior of the mixing process is demonstrated in Fig. 2, showing LEM results for $r_i = 5 \mu\text{m}$, n_0 thermodynamics, and $\varepsilon = 1 \text{ cm}^2 \text{ s}^{-3}$. The initially supersaturated cloudy part (Fig. 2a) is depleted by cloud droplet condensation, resulting in a momentary increase in q_c and the average cloud droplet radius r_m (Figs. 2b and d). Note that our analysis defines cloud droplets as any particle with $r > 0.5 \mu\text{m}$. At the same time, however, the cloud is mixed with its subsaturated surroundings, which decreases S and N_c constantly (Figs. 2a and c). After about 3 s, net condensation switches to evaporation (Fig. 2b), and all droplets evaporate until the end of the simulation, at which a fully subsaturated domain establishes (Figs. 2a and b). Note that for more humid thermodynamic cases (n_1 to n_3), the domain saturates toward the end of the simulation, which prevents the full evaporation of all droplets (not shown).

4.2 Sensitivity on Turbulence Intensity

Now, we assess how changes in the degree of turbulence are captured by the models. Figures 3a to d show the temporal evolution of the domain-averaged q_v , T , q_c , and S for different ε , but the same $r_i = 5 \mu\text{m}$ and n_1 thermodynamics. For readability, we omit the (\dots) to indicate domain averages in the following. Moreover, line colors indicate ε , and line patterns the analyzed models. Irrespective of ε , DNS data are shown by a thin black line to ease their identification.

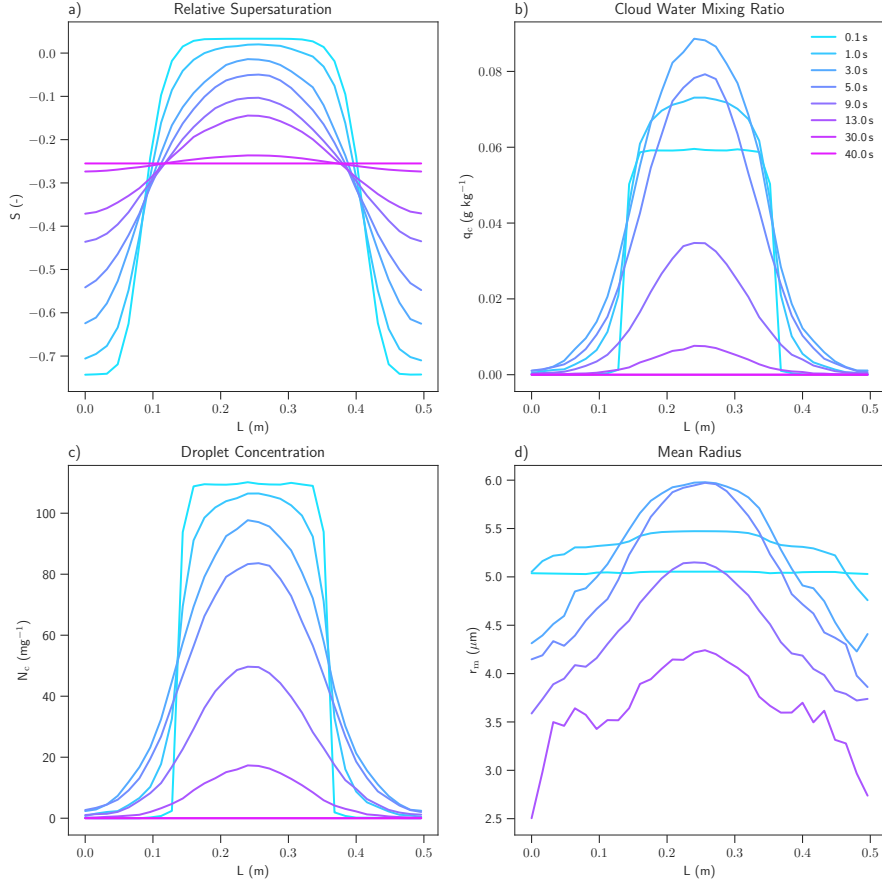


Figure 2. For individual timesteps (blue to green), the development of the relative supersaturation (a), the q_c (b), the droplet concentration (c) and the conditional average of the droplet radius (d) are shown along the entrainment profile. r_m is calculated as an arithmetic mean of an ensemble of 1000 simulation runs, where only gridboxes that contain at least one particle are taken into account.

As discussed for Fig. 2, the initially supersaturated cloudy part causes condensation during the onset of the simulation, resulting in a momentary reduction in q_v (Fig. 3a), a release of latent heat (Fig. 3b), an increase in q_c (Fig. 3c), and a decrease in S (Fig. 3d). The initial condensation is followed by the complete evaporation of all droplets, and a domain void of q_c at the end of the simulation (Fig. 3c). As for the initial condensation phase, the timescale for this process is determined by ε , which determines how quickly the cloud mixes with the ambient air. Specifically, the strongest $\varepsilon = 1000 \text{ cm}^2 \text{ s}^{-3}$ leads to complete evaporation within 3 s, while the smallest $\varepsilon = 1 \text{ cm}^2 \text{ s}^{-3}$ allows the cloud to survive for 20 s.

Overall, the above-described behavior is captured by all models, with minor differences in the mixing rate. These are probably due to slight disagreements in the representation of a specific turbulence intensity, but much smaller than those caused by the

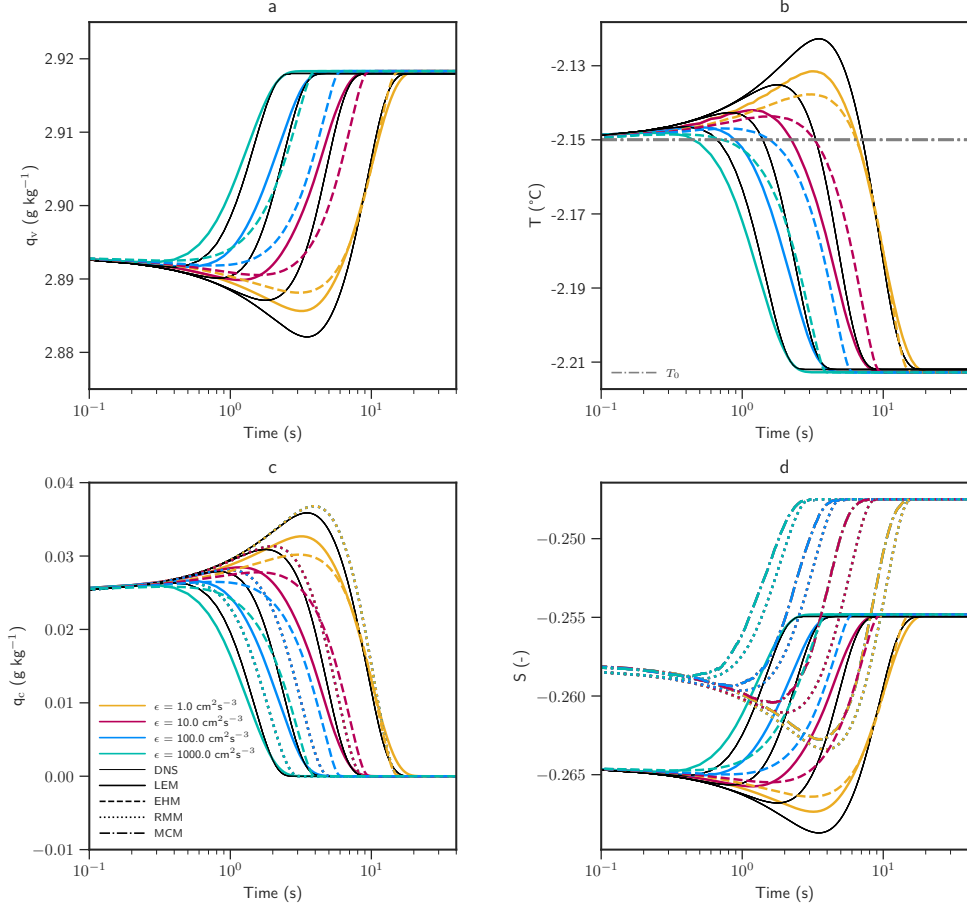


Figure 3. Time evolution of the domain-averaged, that is, arithmetic mean of all grid boxes, (a) q_v , (b) T , (c) q_c and (d) S , for four different energy dissipation rates (colors), and five models (pattern). Note that the DNS results are always in black to highlight them.

analyzed variations in ϵ . Moreover, we see a distinct offset in S predicted by RMM and MCM (Fig. 3d). Because DNS did not provide a domain-averaged S , S is determined from the domain-averaged q_v and T for DNS, LEM, and EHM. On the other hand, RMM and MCM do not predict q_v and T , but S directly. Thus, the offset is a result of the non-linear dependency of S on T that is not appropriately considered when a domain-averaged T is used to determine the domain-averaged S . However, this discrepancy has no impact on the simulated physics, as the time series for q_c suggests (Fig. 3c).

Figures 4a and b show the domain-averaged N_c and r_m , respectively. While r_m increases during the initial condensation phase, N_c remains at its initial value. In the evaporation phase, all models show a decrease in r_m , with full evaporation toward the end of the simulation. Interestingly, DNS, LEM, RMM, and MCM show a gradual decrease in N_c , while EHM predicts a constant N_c until r_m reaches 0. This behavior indicates that DNS, LEM, RMM, and MCM can represent inhomogeneous mixing, which is characterized by a decrease in N_c due to the full evaporation of some droplets during the mixing process. EHM, however, seems to be biased toward homogeneous mixing, during which all droplets evaporate simultaneously, but none fully, resulting in a constant N_c as long as not all droplets evaporate completely.

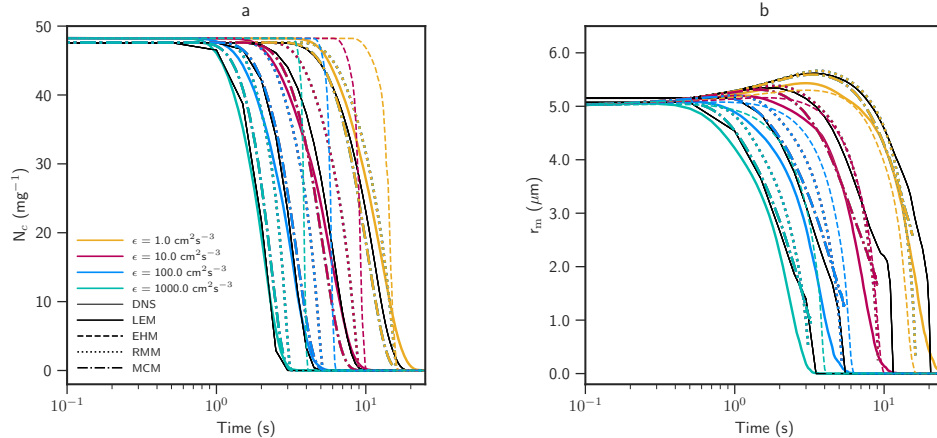


Figure 4. Time evolution of the domain-averaged, that is, arithmetic mean of all grid boxes, (a) N_c , (b) r_m for four different energy dissipation rates (colors), and five models (pattern). Note that the DNS results are always in black to highlight them.

4.3 Sensitivity on Ambient Humidity

Next, we test the susceptibility of all models to different ambient humidities, represented by the thermodynamic cases n_0 to n_3 , all with $r_i = 15 \mu\text{m}$ and $\varepsilon = 33.75 \text{ cm}^2 \text{ s}^{-3}$. Particularly, we investigate cases in which the cloud does not fully evaporate by the end of the simulation (cases n_1 to n_3). As above, Fig. 5 displays the temporal evolution of the domain-averaged q_v , T , q_c , and S . Again, all models capture the behavior well. Note, however, that differences among the models are less visible than for Sec. 4.2 due to the larger range of values covered in the respective ordinates. Particularly, the above-discussed offset in S from RMM and MCM is still present, as well as the same minor variability in the mixing rate. By the end of the mixing process, however, all models agree. This is not surprising since the end state is solely determined by thermodynamics, i.e., all models should reach the same state irrespective of cloud microphysics and dynamics. For RMM and MCM, however, this is only possible since the variability in T is sufficiently small (Fig. 5b) to not violate the underlying assumption of a constant T_0 to determine S .

In Figs. 6a and b, the domain-averaged N_c and r_m are shown. While most models show again a very good agreement with the DNS, we still see that the EHM is not capable of capturing the gradual decrease in N_c but rather represents an abrupt drop when all droplet evaporate. This effect is especially apparent for n_0 (orange lines) where the strongest evaporation takes place, but also for n_1 (red lines). As before, this indicates a bias toward homogeneous mixing in the EHM, while all other models indicate more inhomogeneous mixing.

4.4 Supersaturation Spectra and Droplet Size Distributions

The ability of the presented models to represent the mixing process breaks down to their ability to accurately capture the development of S and hence each droplets' growth history. For $\varepsilon = 1$ and $1000 \text{ cm}^2 \text{ s}^{-3}$, the thermodynamics n_1 , and $r_i = 5 \mu\text{m}$, Lagrangian supersaturation spectra and the corresponding droplet size distributions are presented in Figs. 7 and 8. Here, the term Lagrangian supersaturation refers to the supersaturations experienced by droplets.

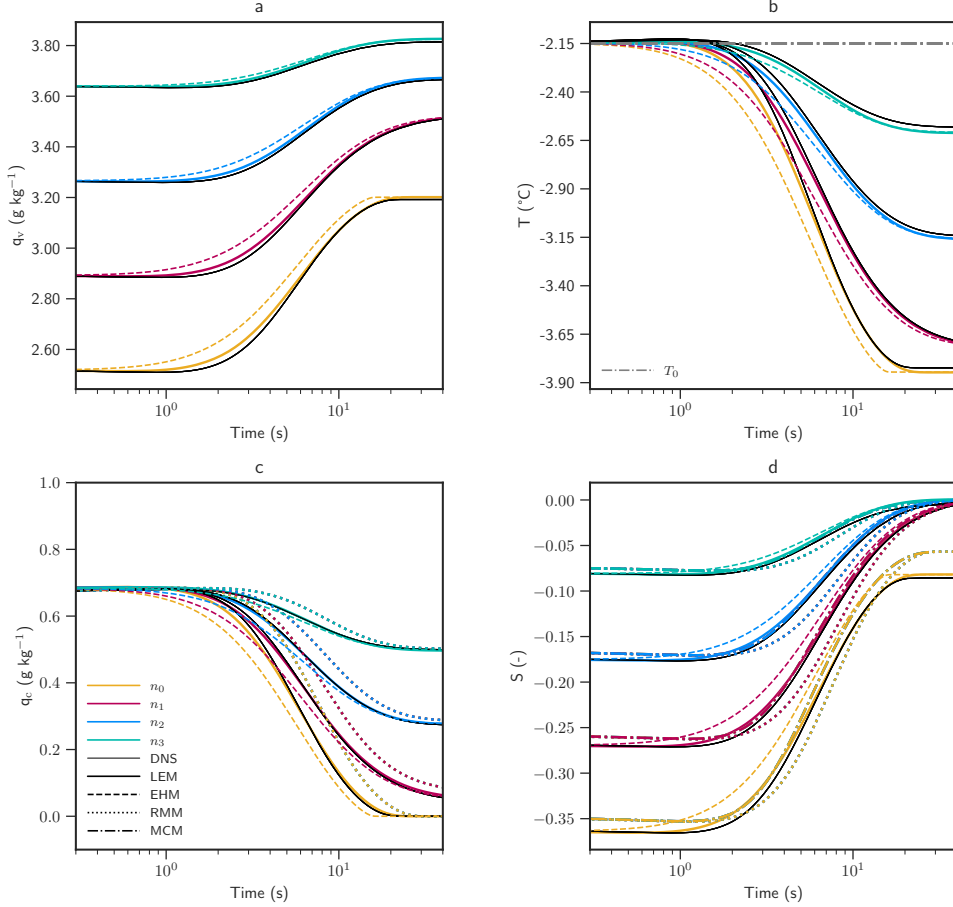


Figure 5. Time evolution of the domain-averaged, (a) q_v , (b) T , (c) q_c and (d) S for four different ambient humidities (colors), and five models (patterns). Note that the DNS results are always in black to highlight them. In (b) the reference temperature T_0 is shown (grey dashed-dotted line)

During the onset of the mixing process (1 s), DNS and LEM show an asymmetric S distribution, consisting of high S from the cloud, and lower ambient S experienced by those droplets already mixed outside of the cloud (Figs. 7a and c, and Figs. 8a and c). As expected, the mode of the S distribution shifts to lower values as the mixing evolves. At the same time, the S distribution also narrows, indicating the homogenization of cloudy and ambient air, resulting in a more Gaussian distribution of S . This behavior is especially visible for $\varepsilon = 1000 \text{ cm}^2 \text{ s}^{-3}$ where mixing is stronger (Fig. 8), while the case with $\varepsilon = 1 \text{ cm}^2 \text{ s}^{-3}$ maintains a broader and more asymmetric distribution throughout the mixing process (Fig. 7). As the MCM relaxes to a Gaussian S distribution by design, it fails to represent the later S distributions for $\varepsilon = 1 \text{ cm}^2 \text{ s}^{-3}$ (Fig. 7e), while it agrees well with the DNS for $\varepsilon = 1000 \text{ cm}^2 \text{ s}^{-3}$ (Fig. 8e). RMM and EHM largely fail to represent the broadening of the S distribution (Figs. 7g and i, and Figs. 8g and i). While EHM assumes a very narrow S distribution that slightly shifts to smaller values, RMM is at least able to represent some asymmetry in the S distribution by including high S from inside the cloud, but it misses representing the lowest ambient S found in DNS.

DNS, LEM, and MCM also agree well in their representation of the droplet size distribution, which contains large droplets from inside the cloud, and smaller droplets

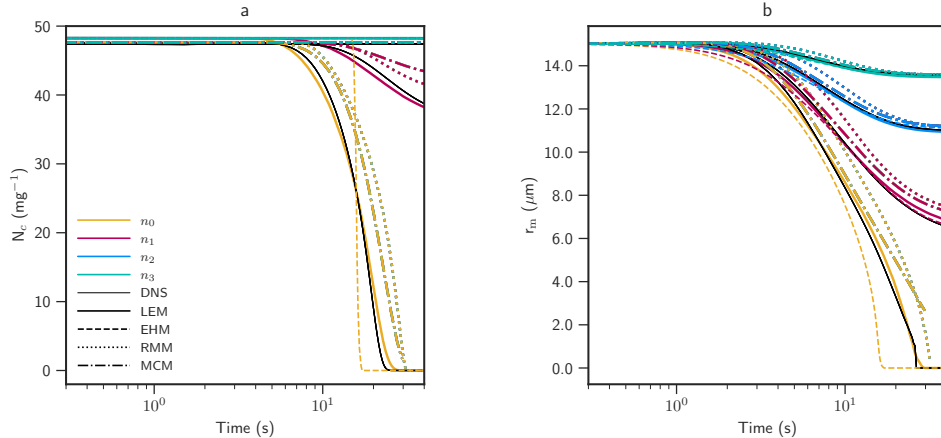


Figure 6. Time evolution of the domain-averaged, (a) N_c , (b) r_m , for four different ambient humidities (colors), and five models (patterns). Note that the DNS results are always in black to highlight them.

that have experienced some mixing and evaporation (Figs. 7b, d, and f, and Figs. 8b, d, and f). Thus, these models are able to represent inhomogeneous mixing during which some droplets evaporate, while others remain (almost) unblemished. The foundation for this is the ability of these models to represent a broad S distribution (Figs. 7a, c, and e, and Figs. 8a, c, and e), as also recently shown by Lim and Hoffmann (2024). The RMM is able to capture this development of the droplet size distribution partially, although the largest droplets evaporate too fast (Figs. 7h and 8h). The EHM shows again a more homogeneous response, where the entire droplet size distribution evaporates to smaller sizes (Fig. 7j and Fig. 8j). Note that these differences among the models are especially strong for $\varepsilon = 1 \text{ cm}^2 \text{ s}^{-3}$ (Fig. 7), which favor inhomogeneous mixing due to the low turbulence intensity, while the differences are smaller for $\varepsilon = 1000 \text{ cm}^2 \text{ s}^{-3}$ (Fig. 8), which mixes more homogeneously.

5 Discussion

Extending our previous analysis, we now discuss some aspects of the individual models that need to be considered for their (potential) utilization as a subgrid-scale scheme.

5.1 “A Posteriori” Nature of the EHM

To represent the thermodynamic development correctly, the EHM needs to be tuned by adjusting the parameters $C_{\text{EHM},1}$ and $C_{\text{EHM},2}$ that steer the impact of mixing and cloud microphysics, as also noted by Saito et al. (2021). For this study, we determined $C_{\text{EHM},1} = 0.18$ and $C_{\text{EHM},2} = 0.03$ as useful tuning parameters for all assessed cases. However, different sets of tuning parameters might be necessary for more different environments that are encountered when the EHM is used as a subgrid-scale model in LES. Interactively adjusting $C_{\text{EHM},1}$ and $C_{\text{EHM},2}$ for a given environment is a challenge that needs to be addressed to further improve the applicability of the EHM as a subgrid-scale model.

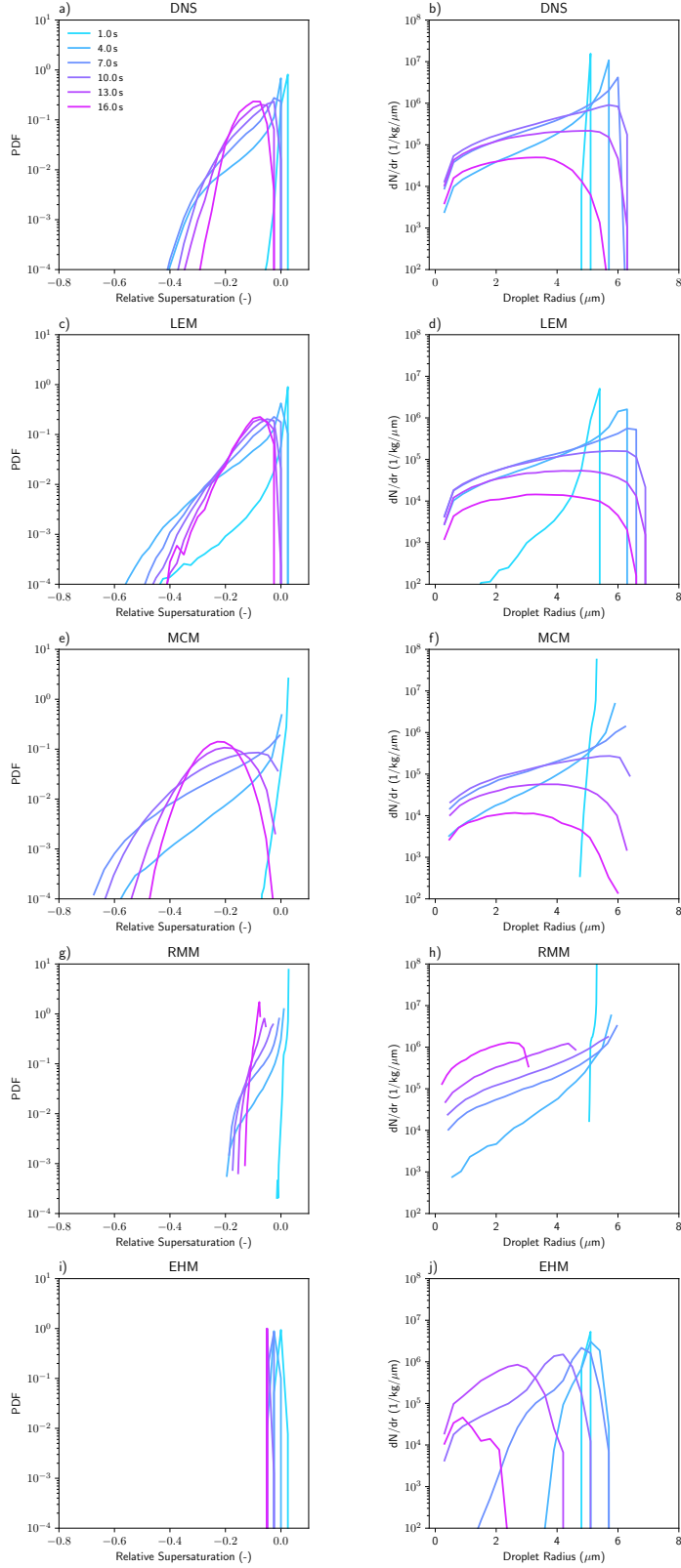


Figure 7. Time evolution of the supersaturation spectra (left column) and droplet size distributions (right column) with n_1 thermodynamics, $r_1 = 5 \mu\text{m}$, and $\varepsilon = 1 \text{ cm}^2 \text{ s}^{-3}$. Different colors represent individual timesteps during the mixing process.

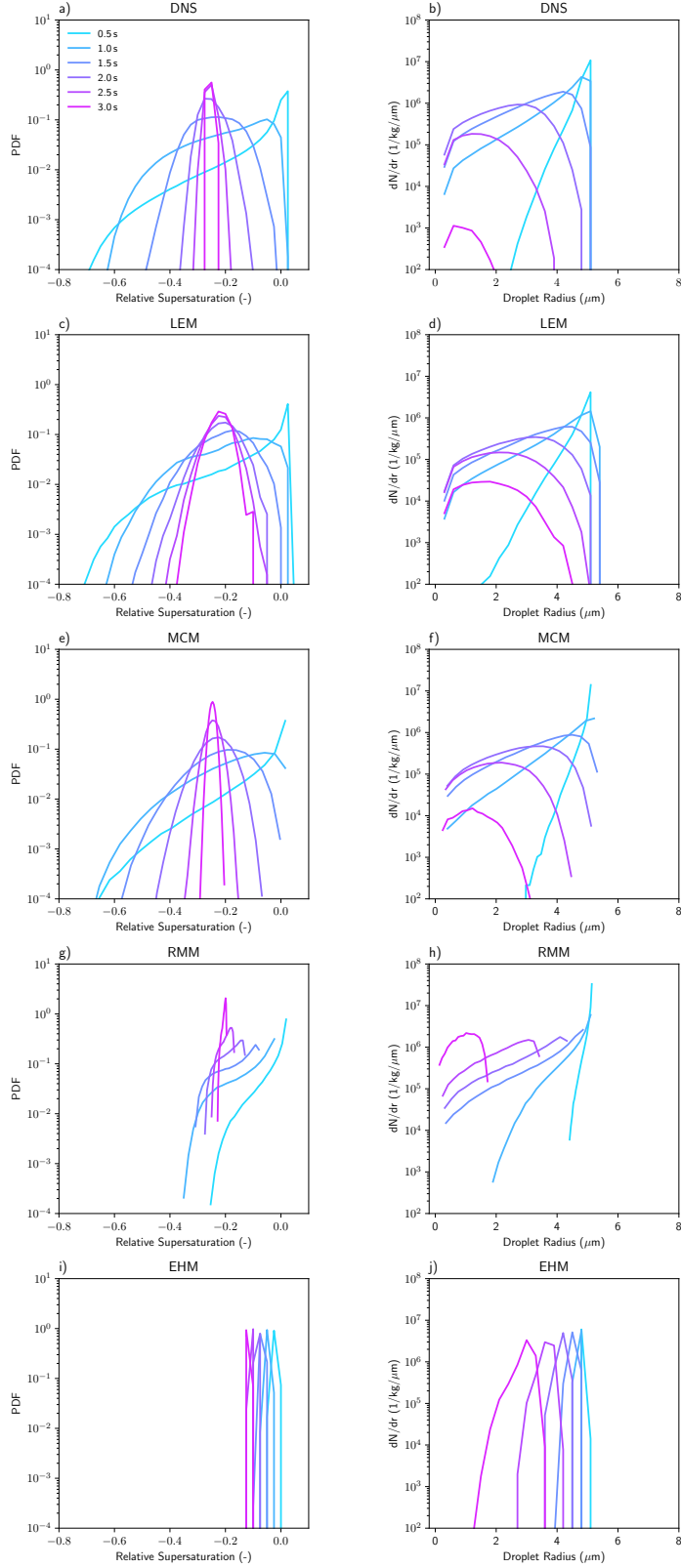


Figure 8. Time evolution of the supersaturation spectra (left column) and droplet size distributions (right column) with n_1 thermodynamics, $r_1 = 5 \mu\text{m}$, and $\varepsilon = 1000 \text{cm}^2 \text{s}^{-3}$. Different colors represent individual timesteps during the mixing process.

5.2 LEM’s Resolution Dependency

To represent turbulence down to η , the LEM resolution is required to be smaller than $\eta/6$ (e.g., Menon & Kerstein, 2011). Although the LEM requires substantially less computational resources than DNS, the high resolution required by the aforementioned constrain can make LEM relatively costly to operate. Thus, it is customary to apply the LEM at lower resolutions, for which D_κ and D_ν are increased appropriately (e.g., Krueger et al., 1997). However, a lower resolution limits the ability of the LEM to represent the details of small-scale mixing.

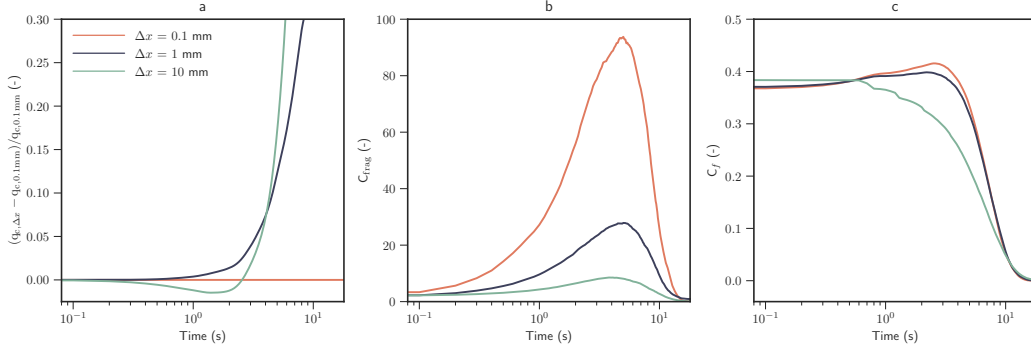


Figure 9. Time series of (a) the relative q_c difference, (b) the fragmentation of the cloud C_{frag} , and (c) the cloud fraction C_f for different LEM resolutions (line colors).

Figure 9 addresses some impacts when a lower LEM resolution is chosen for $\varepsilon = 1 \text{ cm}^2 \text{ s}^{-3}$, $r_1 = 5 \mu\text{m}$, and n_1 thermodynamics. The simulations are run with LEM grid spacings $\Delta x = 0.1, 1.0,$ and 10 mm. Figure 9a shows the relative q_c difference from the highest resolution run, i.e., $(q_{c,\Delta x} - q_{c,0.1\text{mm}})/q_{c,0.1\text{mm}}$, with the additional subscript indicating the resolution. One sees clearly that a larger grid spacing first decelerates initial condensation, resulting in a lower q_c , and then slows down the subsequent evaporation of the cloud, maintaining a higher q_c (cf. Fig. 3c). The deceleration of initial condensation can be attributed to the faster decrease in cloud fraction C_f at coarser resolutions, shown in Fig. 9c and determined from the fraction of grid boxes with $q_c > 10^{-2} \text{ g kg}^{-1}$. Here, the larger grid spacing combined with the up-scaled D_κ and D_ν enables ambient air to be transported deeper into the cloud, where it decelerates the initial condensation. At the same time, the higher D_κ and D_ν artificially moisten the ambient air. This slows down the subsequent evaporation at coarser resolutions. This interpretation is supported by the higher cloud fragmentation C_{frag} at higher resolutions, shown in Fig. 9b and determined from the number of patches with continuously cloudy grid boxes. (To avoid overestimating C_{frag} at high resolutions, the LEM data is coarse-grained using the average distance between two cloud droplets inside the cloud part, about 2 mm.) While C_{frag} remains small during the initial condensation, it quickly increases during evaporation at higher resolutions, indicating a highly intermittent cloud with cloudy patches exposed to (almost unprocessed) ambient air, leading to faster evaporation of some droplets at higher resolution. This analysis indicates that the ability of the LEM to represent inhomogeneous mixing depends on the resolution.

5.3 The Closure-Dependency of MCM

Although EHM, RMM, and MCM exhibit strong similarities in their formulation (cf. Pope, 2011), only MCM captures the development of cloud microphysics during the mixing successfully. To achieve this, MCM requires input from DNSs or other sources

to consider the spatial variability in S , which is not considered in EHM and RMM. Thus, external data needs to be produced for various environments that are encountered during the (potential) application of MCM as a subgrid scale model. Here, machine learning could help to generate closures dependent on the environments experienced in a LES (e.g., Frezat et al., 2022; Jakhar et al., 2024). A similar approach might be possible to estimate the tuning parameters for EHM in Sec. 5.1.

6 Summary and Conclusion

In this study, we assessed the ability of four statistical turbulence models (the LEM, EHM, RMM, and MCM) to represent the small-scale mixing of cloudy and cloud-free air by comparison with DNS data.

The DNS is treated as ground truth, as it directly solves the underlying Navier-Stokes equations (Kumar et al., 2014, 2017). The LEM employs a mapping approach to mimic how turbulence stretches and folds scalars, i.e., the thermodynamic quantities that drive the condensation and evaporation of cloud droplets during the mixing process (Kerstein, 1988; Krueger, 1993). The EHM uses a spatially homogeneous Ornstein-Uhlenbeck process to determine the development of thermodynamics (Pope, 1994; Grabowski & Abade, 2017), while RMM is able to consider some spatial variability of thermodynamic quantities during the mixing process (Pope, 2000; Fries et al., 2021). The MCM uses a mapping closure to predict the non-Gaussian development of thermodynamics during mixing from Gaussian statistics (Chen et al., 1989; Pope, 1991; Fries et al., 2023). All models use a similar Lagrangian representation of cloud microphysics.

All statistical turbulence models accurately capture the development of thermodynamics during the mixing process. However, there are differences in the cloud microphysical properties. The differences are traced down to the ability of the statistical turbulence models to represent the supersaturation history experienced by the cloud droplets. We showed that this history is closely linked to the spatial variability of the supersaturation during the mixing process, which contains subsaturations from ambient air as well as supersaturations from the cloud. Only if this broad distribution of supersaturations and its development is represented in a model, it is able to represent inhomogeneous mixing during which some droplets evaporate completely while others are largely unaffected (Baker & Latham, 1979; Lim & Hoffmann, 2024). This is the case for LEM, MCM, and partially RMM. The EHM, however, fails to represent this aspect of the mixing process, as all droplets experience approximately the same subsaturation. The resultant constant droplet number concentration can be interpreted as homogeneous mixing.

We have demonstrated that simpler and more computationally efficient models can also capture certain aspects of small-scale cloud-edge mixing. Nevertheless, DNS remains essential for accurately resolving the intricate physical processes that are beyond the scope of these models. However, the applicability of LEM, EHM, RMM, and MCM as subgrid-scale models in LES needs to be evaluated further. LEM and EHM are already used as subgrid-scale models to represent the effects of turbulent supersaturation fluctuations on droplet growth in LESs (Hoffmann & Feingold, 2019; Chandrakar et al., 2021). However, for the use of MCM as a subgrid-scale model, some problems need to be solved (e.g., the generation of highly scenario-specific closure data). Nonetheless, the statistical turbulence models analyzed here constitute practicable means to bridge the gap between small-scale turbulence and clouds, and thus constitute a path forward to assess the role of clouds in the climate system in a more holistic framework.

7 Open Research

The model data for this study can be obtained from Kainz et al. (2024). The models are available from the respective authors upon request.

Acknowledgments

J. Kainz and F. Hoffmann were supported by the Emmy Noether program of the German Research Foundation (DFG) under Grant HO 6588/1-1. G. Sardina and B. Mehlig acknowledges support from Vetenskapsrådet (VR) under grant no. 2022-03939, and their computations were enabled by resources provided by the National Academic Infrastructure for Supercomputing in Sweden (NAISS), partially funded by the Swedish Research Council through grant agreement no. 2022-06725. B. Mehlig was also supported by VR under grant no. 2021-4452. The DNS work by B. Kumar, N. N. Makwana, and S. Ravichandran has been carried out using High Performance Computing system (HPCS) facility available at IITM. The IITM is fully funded by the Ministry of Earth Sciences, Government of India. SR is also supported through the Monsoon Mission project IITM/MM-III/2023/IND-4.

References

- Abade, G. C., Grabowski, W. W., & Pawlowska, H. (2018). Broadening of cloud droplet spectra through eddy hopping: Turbulent entraining parcel simulations. *Journal of the Atmospheric Sciences*, *75*(10), 3365 - 3379. Retrieved from <https://journals.ametsoc.org/view/journals/atsc/75/10/jas-d-18-0078.1.xml> doi: 10.1175/JAS-D-18-0078.1
- Baker, M. B., & Latham, J. (1979). The evolution of droplet spectra and the rate of production of embryonic raindrops in small cumulus clouds. *Journal of Atmospheric Sciences*, *36*(8), 1612 - 1615. Retrieved from https://journals.ametsoc.org/view/journals/atsc/36/8/1520-0469_1979_036_1612_teodsa_2_0_co_2.xml doi: 10.1175/1520-0469(1979)036<1612:TEODSA>2.0.CO;2
- Beals, M., Fugal, J., Shaw, R., Lu, J., Spuler, S., & Stith, J. (2015). Holographic measurements of inhomogeneous cloud mixing at the centimeter scale. *Science*, *350*(6256), 87–90.
- Bec, J., Gustavsson, K., & Mehlig, B. (2024). Statistical models for the dynamics of heavy particles in turbulence. *Annual Review of Fluid Mechanics*, *56*, 189-213.
- Bodenschatz, E., Malinowski, S. P., Shaw, R. A., & Stratmann, F. (2010). Can we understand clouds without turbulence? *Science*, *327*(5968), 970-971. Retrieved from <https://www.science.org/doi/abs/10.1126/science.1185138> doi: 10.1126/science.1185138
- Chandrakar, K. K., Grabowski, W. W., Morrison, H., & Bryan, G. H. (2021). Impact of entrainment mixing and turbulent fluctuations on droplet size distributions in a cumulus cloud: An investigation using lagrangian microphysics with a subgrid-scale model. *Journal of the Atmospheric Sciences*, *78*(9), 2983 - 3005. Retrieved from <https://journals.ametsoc.org/view/journals/atsc/78/9/JAS-D-20-0281.1.xml> doi: 10.1175/JAS-D-20-0281.1
- Chen, H., Chen, S., & Kraichnan, R. (1989). Probability distribution of a stochastically advected scalar field. *Phys. Rev. Lett.*, *63*(24), 2657.
- Deardorff, J. W. (1980). Cloud top entrainment instability. *Journal of Atmospheric Sciences*, *37*(1), 131 - 147. Retrieved from https://journals.ametsoc.org/view/journals/atsc/37/1/1520-0469_1980_037_0131_ctei_2_0_co_2.xml doi: 10.1175/1520-0469(1980)037<0131:CTEI>2.0.CO;2
- Frezat, H., Le Sommer, J., Fablet, R., Balarac, G., & Lguensat, R. (2022). A posteriori learning for quasi-geostrophic turbulence parametrization. *Journal of Advances in Modeling Earth Systems*, *14*(11), e2022MS003124. Retrieved from <https://agupubs.onlinelibrary.wiley.com/doi/abs/10.1029/2022MS003124> (e2022MS003124 2022MS003124) doi: <https://doi.org/10.1029/2022MS003124>

- Fries, J., Sardina, G., Svensson, G., & Mehlig, B. (2021). Key parameters for droplet evaporation and mixing at the cloud edge. *Quarterly Journal of the Royal Meteorological Society*, *147*(737), 2160-2172. doi: <https://doi.org/10.1002/qj.4015>
- Fries, J., Sardina, G., Svensson, G., Pumir, A., & Mehlig, B. (2023, Dec). Lagrangian supersaturation fluctuations at the cloud edge. *Phys. Rev. Lett.*, *131*, 254201. Retrieved from <https://link.aps.org/doi/10.1103/PhysRevLett.131.254201> doi: 10.1103/PhysRevLett.131.254201
- Grabowski, W. W., & Abade, G. C. (2017). Broadening of cloud droplet spectra through eddy hopping: Turbulent adiabatic parcel simulations. *Journal of the Atmospheric Sciences*, *74*(5), 1485 - 1493. Retrieved from <https://journals.ametsoc.org/view/journals/atsc/74/5/jas-d-17-0043.1.xml> doi: 10.1175/JAS-D-17-0043.1
- Hoffmann, F. (2023). The small-scale mixing of clouds with their environment: Impacts on micro-and macroscale cloud properties. *Clouds and Their Climatic Impacts: Radiation, Circulation, and Precipitation*, 255-270.
- Hoffmann, F., & Feingold, G. (2019). Entrainment and mixing in stratocumulus: Effects of a new explicit subgrid-scale scheme for large-eddy simulations with particle-based microphysics. *Journal of the Atmospheric Sciences*, *76*(7), 1955 - 1973. Retrieved from <https://journals.ametsoc.org/view/journals/atsc/76/7/jas-d-18-0318.1.xml> doi: 10.1175/JAS-D-18-0318.1
- Jakhar, K., Guan, Y., Mojjani, R., Chattopadhyay, A., & Hassanzadeh, P. (2024). Learning closed-form equations for subgrid-scale closures from high-fidelity data: Promises and challenges. *Journal of Advances in Modeling Earth Systems*, *16*(7), e2023MS003874. Retrieved from <https://agupubs.onlinelibrary.wiley.com/doi/abs/10.1029/2023MS003874> (e2023MS003874 2023MS003874) doi: <https://doi.org/10.1029/2023MS003874>
- Kainz, J., & Hoffmann, F. (2023). The effects of aerosol on small-scale cloud-environment mixing: Implications for simulating and observing inhomogeneous mixing. *Journal of Geophysical Research: Atmospheres*, *128*(22), e2023JD038509. Retrieved from <https://agupubs.onlinelibrary.wiley.com/doi/abs/10.1029/2023JD038509> (e2023JD038509 2023JD038509) doi: <https://doi.org/10.1029/2023JD038509>
- Kainz, J., Nikitabehen N., M., Kumar, B., Ravichandran, S., Fries, J., Sardina, G., ... Hoffmann, F. (2024, October). *Benchmarking Turbulence Models to Represent Cloud-Edge Mixing*. Zenodo. Retrieved from <https://doi.org/10.5281/zenodo.13813360> doi: 10.5281/zenodo.13813360
- Kerstein, A. R. (1988). A linear-eddy model of turbulent scalar transport and mixing. *Combustion Science and Technology*, *60*(4-6), 391-421. Retrieved from <https://doi.org/10.1080/00102208808923995> doi: 10.1080/00102208808923995
- Krueger, S. K. (1993). Linear eddy modeling of entrainment and mixing in stratus clouds. *Journal of the atmospheric sciences*, *50*(18), 3078-3090.
- Krueger, S. K., & Kerstein, A. R. (2018). An economical model for simulating turbulence enhancement of droplet collisions and coalescence. *Journal of Advances in Modeling Earth Systems*, *10*(8), 1858-1881.
- Krueger, S. K., Su, C.-W., & McMurtry, P. A. (1997). Modeling entrainment and finescale mixing in cumulus clouds. *Journal of the atmospheric sciences*, *54*(23), 2697-2712.
- Kumar, B., Bera, S., Parabhakaran, T., & Grabowski, W. W. (2017). Cloud-edge mixing: Direct numerical simulation and observations in indian monsoon cloud. *Journal of Advancing in Modeling Earth Systems*, *9*, 332-353. doi: 10.1002/2016MS000731
- Kumar, B., Janetzko, F., Schumacher, J., & Shaw, R. A. (2012). Extreme responses

- of a coupled scalar-particle system during turbulent mixing. *New Journal of Physics*, *14*(11), 115020. doi: 10.1088/1367-2630/14/11/115020
- Kumar, B., Schumacher, J., & Shaw, R. A. (2013). Cloud microphysical effects of turbulent mixing and entrainment. *Theor. Comput. Fluid Dyn.*, *27*, 361–376.
- Kumar, B., Schumacher, J., & Shaw, R. A. (2014). Lagrangian mixing dynamics at the cloudy-clear air interface. *Journal of Atmospheric Sciences*, *71*(7), 2564–2580. doi: 10.1175/JAS-D-13-0294.1
- Lim, J.-S., & Hoffmann, F. (2024). Life cycle evolution of mixing in shallow cumulus clouds. *Journal of Geophysical Research: Atmospheres*, *129*(10), e2023JD040393.
- Menon, S., & Kerstein, A. R. (2011). The linear-eddy model. In T. Echehki & E. Mastorakos (Eds.), *Turbulent combustion modeling: Advances, new trends and perspectives* (pp. 221–247). Dordrecht: Springer Netherlands. Retrieved from https://doi.org/10.1007/978-94-007-0412-1_10 doi: 10.1007/978-94-007-0412-1_10
- Moin, P., & Mahesh, K. (1998). Direct numerical simulation: a tool in turbulence research. *Annual review of fluid mechanics*, *30*(1), 539–578.
- Pope, S. (1991). Mapping closures for turbulent mixing and reaction. *Theor. Comput. Fluid Dyn.*, *2*(5), 255–270.
- Pope, S. (1994). Lagrangian pdf methods for turbulent flows. *Annu. Rev. Fluid Mech.*, *26*, 23–63.
- Pope, S. (2000). *Turbulent Flows*. Cambridge University Press.
- Pope, S. (2011). Simple models of turbulent flows. *Phys. Fluids*, *23*(1), 011301.
- Rogers, R. R., & Yau, M. K. (1989). *A short course in cloud physics* (3rd ed.). Butterworth-Heinemann.
- Saito, I., Watanabe, T., & Gotoh, T. (2021). Statistical properties of a stochastic model of eddy hopping. *Atmospheric Chemistry and Physics*, *21*(17), 13119–13130. Retrieved from <https://acp.copernicus.org/articles/21/13119/2021/> doi: 10.5194/acp-21-13119-2021
- Smagorinsky, J. (1963). General circulation experiments with the primitive equations: I. the basic experiment. *Monthly Weather Review*, *91*(3), 99–164. Retrieved from https://journals.ametsoc.org/view/journals/mwre/91/3/1520-0493_1963_091_0099_gcewtp_2_3_co_2.xml doi: 10.1175/1520-0493(1963)091<0099:GCEWTP>2.3.CO;2
- Uhlenbeck, G. E., & Ornstein, L. S. (1930). On the theory of the brownian motion. *Physical Review*, *36*, 823–841.
- Vaillancourt, P., Yau, M., & Grabowski, W. W. (2001). Microscopic approach to cloud droplet growth by condensation. part i: Model description and results without turbulence. *Journal of the atmospheric sciences*, *58*(14), 1945–1964.